CrossMark

Nanoengineered three-dimensional hybrid Fe_2O_3@PPy nanotube arrays with enhanced electrochemical performances as lithium–ion anodes

Hongyan Yang[1] · Xiaohui Yu[1] · Haowen Meng[1] · Peng Dou[1] · Daqian Ma[1] · Xinhua Xu[1,2]

Abstract In order to optimize the electrode system of lithium–ion batteries (LIBs) for problems like lithium-ion diffusion, electron transport, and large volume change during cycling processes, a novel three-dimensional (3D) hybrid Fe_2O_3 nanotube array anode coated by polypyrrole (Fe_2O_3@PPy) is synthesized via a sacrificial template-accelerated hydrolysis method followed by a chemical vapor-phase polymerization process. In the hollow core–shell nanostructures, the conducting PPy layer could not only facilitate the electron transport, but also force the core to expand inward into the hollow space, which allows for free volume expansion of the Fe_2O_3 without mechanical breaking. Besides, the static outer surface is contributed to form a stable solid electrolyte interface film. As a result, the integration of 3D hybrid nanostructure electrode is capable of retaining a high capacity of 665 mA h g^{-1} after 150 cycles with a coulombic efficiency of above 97 %, revealing better cycling properties compared with bare Fe_2O_3 nanotube arrays' anode. This nanoengineering strategy is proven to be an ideal candidate for the development of high-performance anode for LIBs.

✉ Xinhua Xu
  xhxutju@gmail.com

  Hongyan Yang
  yang_hy@tju.edu.cn

  Xiaohui Yu
  lovingyuxiaohui@163.com

  Haowen Meng
  13820173122@163.com

  Peng Dou
  doupeng2010@163.com

  Daqian Ma
  dqmatju@tju.edu.cn

[1] School of Materials Science and Engineering, Tianjin University, Tianjin 300072, People's Republic of China

[2] Tianjin Key Laboratory of Composite and Functional Materials, Tianjin 300072, People's Republic of China

Introduction

Rechargeable lithium–ion batteries (LIBs) have been the most widely used power source for portable electronic devices due to their long cycling life, high energy, and power density [1, 2]. As a key component, electrode material dominates the electrochemical properties of LIBs. Currently, graphite-based anode is utilized in most commercial rechargeable LIBs. However, it could not meet the increasing needs of power battery application because it can only deliver a theoretical capacity of about 372 mA h g^{-1} [2, 3]. Recently, it has been found that transition metal oxides, such as Fe_2O_3 [4–6], Fe_3O_4 [7], Co_3O_4 [8, 9], SnO_2 [2, 10], and NiO [11] exhibit high reversible capacities, greatly spurring the rapid development of this field. Among these promising anode materials, Fe_2O_3 has long been regarded as an appealing host material for lithium storage due to its high theoretical capacity (1007 mA h g^{-1}), nontoxicity, and low processing cost [5, 12]. However, in spite of these excellent characteristics, Fe_2O_3 suffers from poor conductivity and large volume change in the electrochemical reaction [13–15], which would lead to electrode pulverization and loss of contact with current collector, resulting in a large capacity loss, low initial coulombic efficiency, and poor rate and cycling stability.

Numerous measures are devoted to alleviate mechanical degradation and capacity fading. Among all the methods, an effective approach is structural modification to buffer

volume change during the discharge and charge processes. In particular, three-dimensional (3D) hollow nanotube arrays' electrode has attracted considerable attention due to its large internal void, high surface area, and outstanding permeation [16–18]. The thin shells in hollow nanostructures could provide a fast and efficient transport for both Li^+ and electrons, which contributes to the improved reaction kinetics at the electrode surface [19]. Nevertheless, the electrode may degrade during long-term cycling because the hollow structure without protection would still expand out toward the electrolyte during lithiation, and shrink during delithiation [20]. As a consequence, the solid electrolyte interphase (SEI) film formed during Li^+ insertion would be broken and decomposed completely [21, 22], resulting in the exposure of some fresh active materials to the electrolyte and repeated regeneration of the SEI film, which would cause consumption of abundant Li^+ and a large irreversible capacity (i.e., low coulombic efficiency) [23, 24].

In general, one strategy to obtain the stable SEI film is to create core/shell nanostructures [25, 26]. Liu et al. have successfully prepared a 3D carbon/hematite (C/α–Fe$_2$O$_3$) nanotube arrays' electrode, exhibiting better capacity retention and rate capability compared with the bare 3D Fe$_2$O$_3$ nanotube arrays. Nevertheless, the designed carbon/hematite composite anode is easily reduced to Fe^{2+} or Fe^0 at 600 °C due to its poor thermal stability. Hence, the carbon precursors must be carefully chosen, and the time of carbonization should be prolonged to render moderate electrical conductivity of the components [27]. Recently, a great number of researches have proposed some electronically conducting polymers with high conductivity, chemical stability, and low cost as surface coating layer and/or active matrix [28–31]. Among them, polypyrrole (PPy) is regarded as one of the most attractive conducting polymers [29–31], which could not only lower the charge-transfer resistance in electrochemical reactions, but also prevent the direct contact between active materials and electrolytes. More importantly, the volume expansion of the electrode could be restricted into the PPy coating layer, which is helpful to protect the SEI film from rupturing during delithiation, thus ensuring high coulombic efficiency and long-term stable cycling [20].

Inspired by these needs, we fabricated vertically aligned Fe$_2$O$_3$ nanotube arrays on stainless steel substrate. Furthermore, a conductive PPy additive layer was coated on Fe$_2$O$_3$ via a chemical vapor-phase polymerization to prepare Fe$_2$O$_3$ @PPy electrode. Due to the protection of PPy coating layer, the hollow Fe$_2$O$_3$ nanotube could expand into its internal void space and maintain a static outer surface, which is beneficial for the development of a stable SEI film and the maintenance of a long cycle life. As a result, the Fe$_2$O$_3$@PPy nanotube arrays' electrode delivered higher reversible capacities and superior rate performances compared with the bare Fe$_2$O$_3$ electrode. We believe that the facile synthesis of Fe$_2$O$_3$@PPy nanotube arrays' electrode could be favorably considered as a promising candidate for practical applications among lithium–ion anodes.

Experimental

Materials

All chemicals were analytical grade and used without further purification. Fe(NO$_3$)$_3$·9H$_2$O (>99 %), sodium dodecyl sulfate (SDS), ammonium persulfate (APS) were obtained from Kewei Chemical Reagent Co. Ltd. of Tianjin University (Tianjin, China). Pyyole monomer (98 % reagent grade) was purchased from Sigma Aldrich PTE. Ltd, Singapore. The stainless steel foil (60 μm) was purchased from Shanghai Chemical Reagent Co. Ltd., pretreated by sonication in absolute ethanol and distilled water successively and dried in air at 40 °C.

Preparation of 3D Fe$_2$O$_3$@PPy nanotube arrays on stainless steel substrates

Conventional methods to prepare vertically aligned nanotube arrays have been proposed by template-directed growth with the utilization of ZnO nanorod arrays template as the growth director [32–34]. Herein, we used them to grow Fe$_2$O$_3$ nanotubes on a piece of stainless steel foil via a sacrificial template-accelerated hydrolysis method [35]. In brief, ZnO nanorod arrays [36] were grown on stainless steel foil and placed into a 40 mL aqueous solution containing 0.1 M Fe(NO$_3$)$_3$·9H$_2$O. Then the sample was kept still at room temperature for 12 h. After immersion, it was taken out, dried in air, and treated at 450 °C in argon for 5 h to obtain Fe$_2$O$_3$ nanotube arrays. The PPy coating was conducted by chemical vapor-phase polymerization as follows: the resulting Fe$_2$O$_3$ nanotube arrays were put into a 0.1 mL solution composed of 3 mM APS as the oxidant and 0.15 mM SDS as the dopant, ultrasonicated for a moment and kept still for 30 min at room temperature. After the solution had been absorbed, the nanotube arrays were put into a beaker where a vial containing 20 μL pyrrole monomer was used for generate pyrrole vapor, without direct contact to the sample. After sealing, the beaker was left at room temperature for 15 min. Finally, the product was taken out and washed with deionized water, and dried at 80 °C overnight.

Materials characterization

The crystal structure of the product was determined by grazing incidence X-ray diffraction (GIXRD) using an

automated RIGAKU/DMAX2500 X-ray diffractometer with monochromatic Cu Kα radiation, the 2 theta Bragg angles were scanned over a range of 20°–80° at a rate of 5.0° min^{-1}. The size and morphology of the product were determined by a Hitachi S-4800 field-emission scanning electron microscope (FE-SEM) at an accelerating voltage of 5 kV and a high-resolution transmission electron microscope (HR-TEM, JEM-2100F) operated at 200 kV. Fourier transform infrared (FT-IR) spectra were recorded using an FT-IR analyzer (EQUINOX55). The valence state of iron was investigated by X-ray photoelectron spectroscopy (XPS) (PHI 1600 ESCA system). An Al Kα monochromatized radiation was employed as the X-ray source.

Electrochemical analyses

The electrochemical experiment was performed using coin cells (type CR2032) assembled in an argon-filled dry glove box by directly using the as-prepared bare Fe_2O_3 and Fe_2O_3@PPy nanotube arrays as the positive electrode. For comparison purpose, the pure PPy electrode was fabricated by coating the slurry comprising of 80 wt% PPy, 10 wt% acetylene black and 10 wt% polyvinylidene fluoride (PVDF) onto the stainless steel foil. Li metal foil was utilized as the counter electrode, 1 M $LiPF_6$ in ethylene carbonate (EC) and dimethyl carbonate (DMC) (1:1 by volume) was used as the electrolyte and Celgard 2400 was used as the separator. The galvanostatic charge–discharge measurement and rate performance were performed over the potential range 0.01–3.00 V (versus Li^+/ Li) using a MTI Battery Testing System at room temperature. Electrochemical impedance spectroscopy measurements were performed in an alternating current frequency range from 1 to 1 MHz. The capacities of bare Fe_2O_3 and Fe_2O_3@PPy anode were reported based on the weight of Fe_2O_3.

Results and discussion

The crystallographic structures of bare Fe_2O_3 and Fe_2O_3@PPy nanotube arrays were investigated by grazing incidence X-ray diffraction analysis as shown in Fig. 1a. For curve (1), the diffraction peaks labeled with stars come from the stainless steel foil [37]. The peaks labeled with solid circles located at 24.1°, 33.1°, 35.6°, 40.8°, 49.4°, 54.0°, 57.6°, 62.4°, and 64.0° can be indexed to the standard hematite α-Fe_2O_3 (JCPDS 33-0664), which are assigned to the (012), (104), (110), (113), (024), (116), (018), (214), and (300) lattice planes, respectively. A wide diffraction peak is observed around 21.5°– 28.5° in curve (2), which can be attributed to the amorphous PPy phase [38]. Fe2p XPS high-resolution spectrum was conducted to further confirm the valence state of Fe in the as-prepared nanotube arrays. As observed from Fig. 1b, Fe2p3/2 and Fe2p1/2 appeared at binding energies of about 710.9 and 724.8 eV with a shake-up satellite around 718.8 eV, which are attributed to hematite phase (α-Fe_2O_3) [39].

Figure 2a and b show the scanning electron microscopy (SEM) images of ZnO and Fe_2O_3 nanotube arrays, from which we can confirm that the array structure of ZnO is well maintained after the formation of Fe_2O_3 nanotubes. The columnar nanotubes have closed tips and are assembled from numerous nanoparticles, with outer diameters ranging from 150 to 250 nm (Fig. 2b). In order to measure the length of the nanotubes, the sample was rinsed with deionized water to present the cross section of array on the substrates before annealing at 450 °C. As shown in Fig. 2c, the length of the nanotubes is about 1.18 μm. More evidence about the structure of the product was given by transmission electron microscopy (TEM) analysis. Tubular structures with wall thickness in the range of 50–60 nm and inner diameter of 100 nm can be observed in the inset of Fig. 2b. HRTEM shown in Fig. 2d confirmed that the Fe_2O_3 nanotubes are composed of polycrystalline composition. The distances between the adjacent planes are 0.27,

Fig. 1 **a** XRD patterns of (*i*) bare Fe_2O_3 nanotube arrays and (*ii*) Fe_2O_3@PPy nanotube arrays; **b** XPS high-resolution spectrum of Fe2p core level for bare Fe_2O_3 nanotube arrays
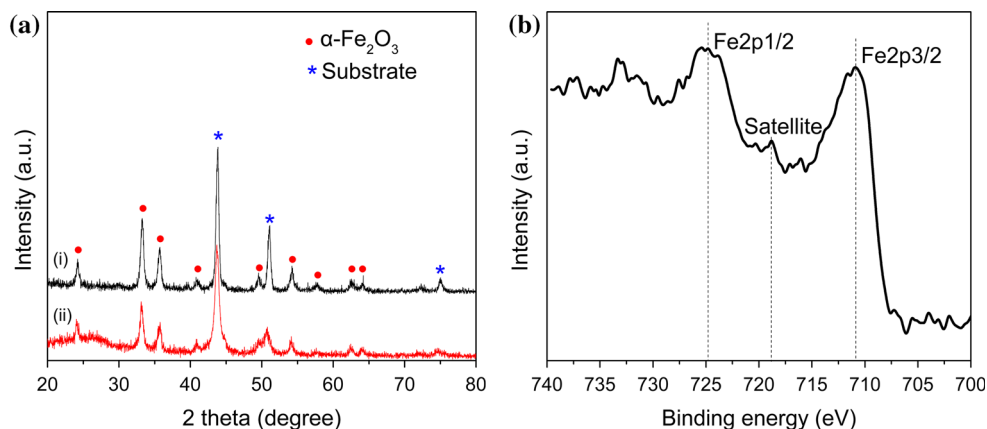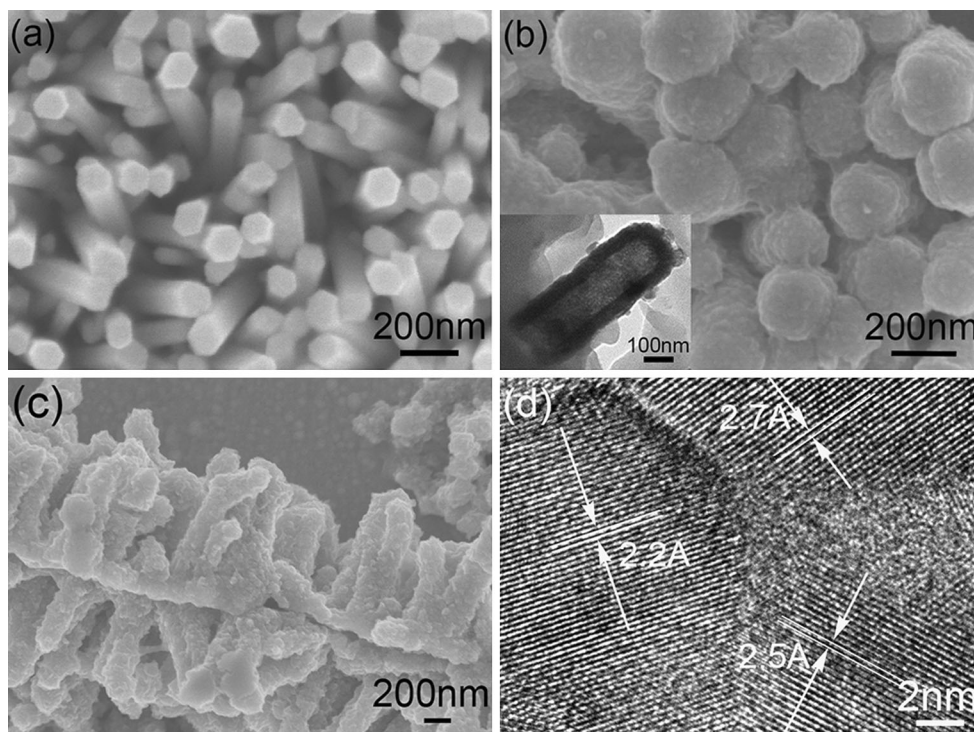
Fig. 2 **a** SEM image of ZnO nanorod arrays; **b** and **c** SEM images of bare Fe_2O_3 nanotube arrays, *inset* in **b** showing the TEM image of Fe_2O_3 nanotube; **d** HRTEM image of Fe_2O_3 nanotube
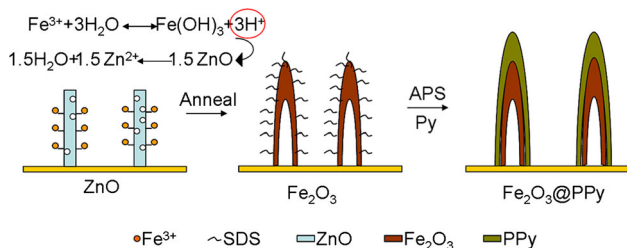

Fig. 3 Schematic illustration of the formation process of Fe_2O_3@PPy nanotube arrays

0.25, and 0.23 nm corresponding to (104), (110), and (113) planes of α-Fe_2O_3, respectively [40]. The results are consistent with XRD.

A schematic depiction for the synthesis of the 3D Fe_2O_3 @PPy nanotube arrays is presented in Fig. 3. The ZnO template was etched by H^+ produced from $Fe(NO_3)_3$ hydrolysis, which in turn accelerated the hydrolysis and acted as a crucial step initiating the construction of the 3D nanotube arrays' architecture. In order to improve the electronic conductivity and the stabilization of SEI film, we designed a thin layer of conducting PPy via a chemical vapor-phase polymerization, which was anchored on the surface of Fe_2O_3 nanotubes uniformly. Figure 4a shows scanning electron microscopy (SEM) images of the Fe_2O_3@PPy nanotube arrays. Obviously, after coating PPy onto the Fe_2O_3 nanotubes,

some big bumps are generated on the surface. PPy is uniformly coated on the surface of each Fe_2O_3 nanotube, and there are some spaces between each pair of nanotubes. The outer diameter of Fe_2O_3@PPy nanotubes is about 200–300 nm. Upon combining with the SEM image of Fe_2O_3 nanotube arrays (Fig. 1c), we could deduce that the thickness of PPy layer is about 20 nm. The TEM image (Fig. 4b) clearly reveals that the nanotubes are uniformly and continuously coated with a thin PPy layer. A small part of the photo, which was denoted by the red rectangle, was chosen for EDS mapping analysis to further distinguish the compositions. As shown in Fig. 4c, C and N have a wider distribution than Fe and O, which is unambiguously illustrated. The molecular structures of the Fe_2O_3@PPy composite were characterized by FT-IR spectroscopy. The characteristic absorptions of the Fe_2O_3@PPy composites are similar to that of the PPy, as presented in Fig. 5, which demonstrates the existence of PPy in the composite. It can be clearly seen that the characteristic peaks of PPy are located at around 1610, 1470, 1398, 1235, 1047, 925, and 800 cm^{-1}, which is in perfect accordance with the literature. The fundamental vibration bands of the PPy ring appear at around 1610, 1470, and 1398 cm^{-1} [41]. The peak at 1235 cm^{-1} is attributed to C–N stretching vibrations [42], at 1045 cm^{-1} to the =C–H in-plane vibrations, and at 925 and 800 cm^{-1} to C–H out-of-plane deformation vibrations of the ring [41].
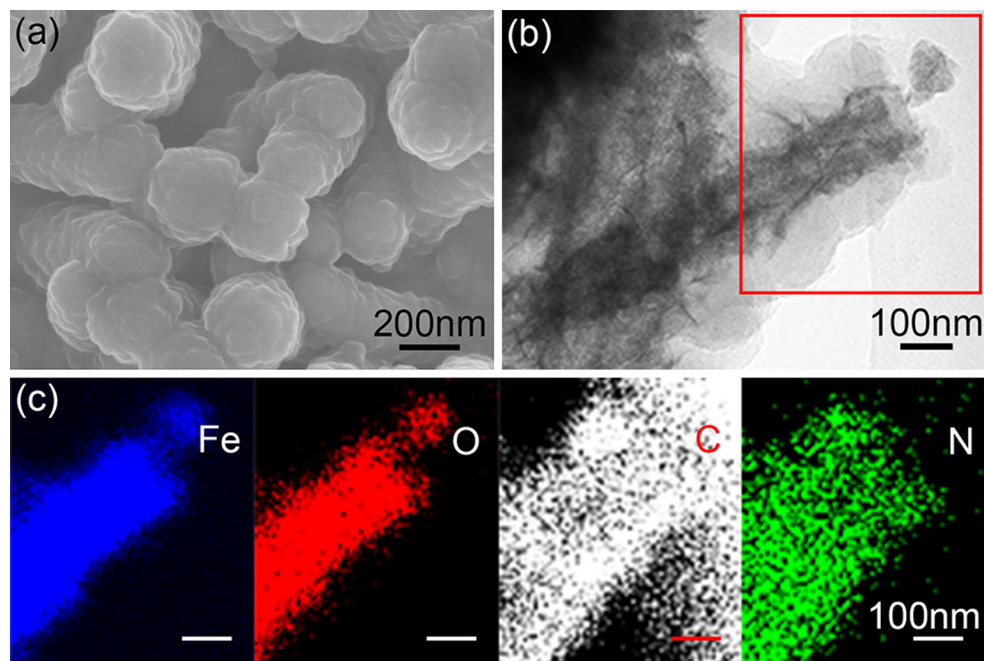
Fig. 4 **a** SEM image of Fe$_2$O$_3$@PPy nanotube arrays; **b** TEM image of Fe$_2$O$_3$@PPy nanotubes; **c** corresponding elemental mappings of Fe, O, C, and N of the selected area in **b**
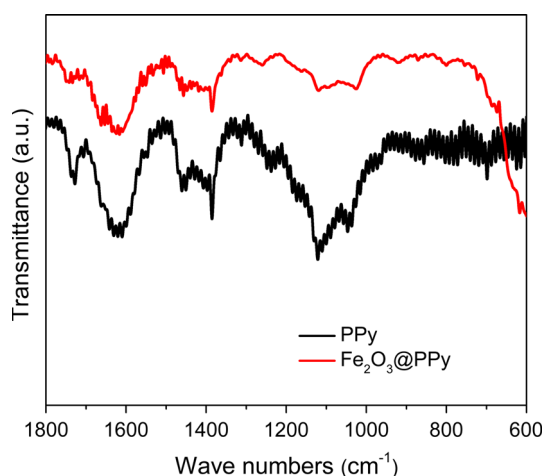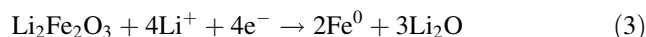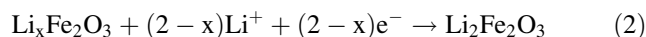

**Fig. 5** FT-IR spectra of pure PPy and Fe$_2$O$_3$@PPy nanotube arrays

The electrochemical cycle performance of the Fe$_2$O$_3$ @PPy nanotube arrays' electrode was evaluated by galvanostatic charge/discharge cycling at a current density of 100 mA g^{-1} from 3.00 to 0.01 V on the basis of the mass of Fe$_2$O$_3$. For comparison, bare Fe$_2$O$_3$ nanotube arrays and pure PPy electrodes were also investigated under the same conditions. The galvanostatic discharge–charge curves of bare Fe$_2$O$_3$ and Fe$_2$O$_3$@PPy nanotube arrays are shown in Fig. 6a and b. The electrochemical behaviors of the two electrodes are similar, which is in general consistency with the literature [43, 44]. For the discharge curve in the first cycle, the voltage initially decreases quickly to

approximately 1.5 V followed by a weak slope, corresponding to the initial lithium insertion into the Fe$_2$O$_3$ [Eq. (1)]. In the next step of lithium intercalation, a wide slope located at 1.2–0.8 V is observed, where there is a phase transformation from the hexagonal Li$_x$Fe$_2$O$_3$ to the cubic Li$_2$Fe$_2$O$_3$ [Eq. (2)]. An obvious plateau is observed at 0.8 V, indicating the complete reduction of iron from Fe^{2+} to Fe^0 [Eq. (3)].

$$Fe_2O_3 + xLi^+ + xe^- \rightarrow Li_xFe_2O_3 \qquad (1)$$

$$Li_xFe_2O_3 + (2 - x)Li^+ + (2 - x)e^- \rightarrow Li_2Fe_2O_3 \qquad (2)$$

$$Li_2Fe_2O_3 + 4Li^+ + 4e^- \rightarrow 2Fe^0 + 3Li_2O \qquad (3)$$

Continuation of the discharge reaction up to the lower cut-off (0.01 V) shows a sloping profile, which can be ascribed to the formation of SEI films along with the decomposition of the electrolyte and further lithium storage via interfacial charging at metal/Li$_2$O interface [44, 45]. The first discharge and charge capacities of Fe$_2$O$_3$@PPy nanotube arrays are 1424 and 1088 mA h g^{-1}, with a higher coulombic efficiency of 76 % compared with the bare Fe$_2$O$_3$ electrode (69 %). During the subsequent cycles, the discharge curves only show a slope at 1.0–0.75 V, and the capacities are reduced, which is caused by the incomplete conversion reaction and irreversible lithium loss due to the formation of the SEI film. The specific capacities from discharge profiles in the 30th and 50th cycles of the bare Fe$_2$O$_3$ electrode have dropped obviously, which is caused by the structural damages of the electrode

Fig. 6 Discharge–charge curves of **a** bare Fe_2O_3 nanotube arrays' electrode and **b** Fe_2O_3@PPy nanotube arrays' electrodes; **c** cycling performance; and **d** coulombic efficiencies of both Fe_2O_3@PPy nanotube arrays' and control electrodes
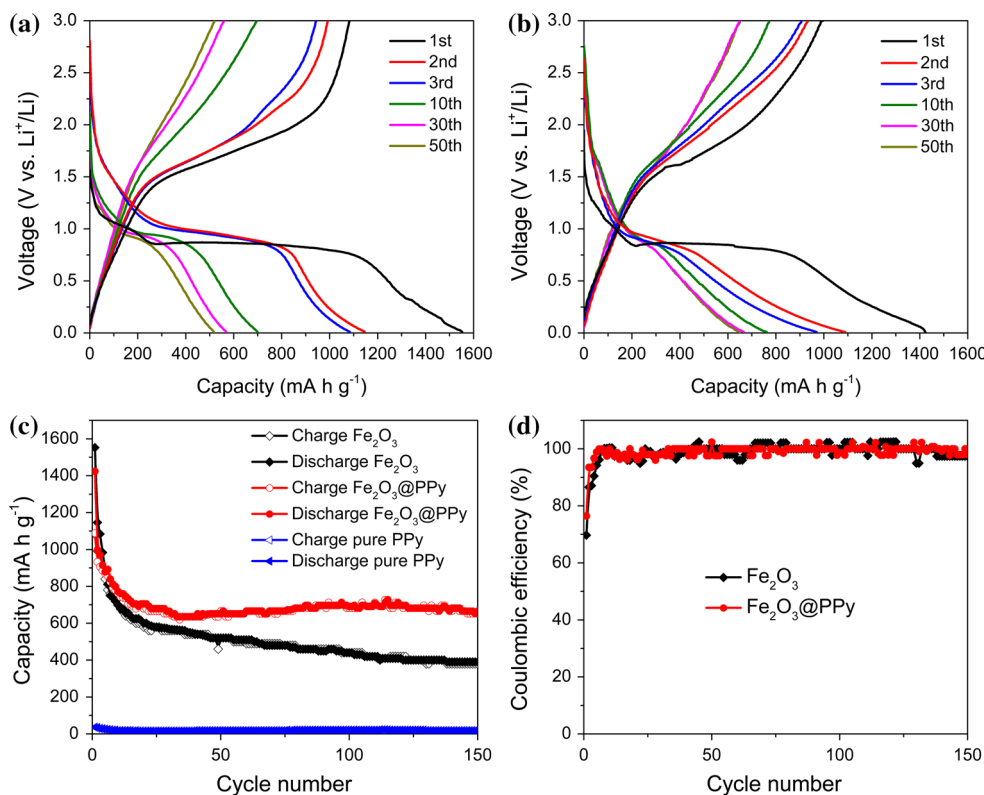
and the continuous formation of the SEI films during cycling. By contrast, the specific capacity of Fe_2O_3@PPy electrode has basically reached a stable value after 30 cycles, and the discharge–charge profiles of the 30th and 50th cycles remain nearly unchanged, demonstrating the compositional and the structural stability of the PPy-coated electrode.

Figure 6c and d show the cycle performance of both Fe_2O_3@PPy and control electrodes. The capacity of the PPy electrode retains only 18 mA h g^{-1} after 10 cycles, in accordance with the literature [38]. Therefore, the low capacity of PPy can be ignored in analysis of Fe_2O_3@PPy anode. Although the initial capacity of bare Fe_2O_3 electrode is 1552 mA h g^{-1}, it declines rapidly in the following cycles and maintains only about 390 mA h g^{-1} after 150 cycles. The poor cycle performance is caused by the unstable SEI film formed during Li^+ insertion, which is decomposed easily, catalyzed by the iron metal formed during the reduction process [21]. On the contrary, the capacity of Fe_2O_3@PPy electrode exceeds that of bare Fe_2O_3 only after five cycles because of its smaller irreversible capacity. Even though the capacity decays gradually in the first 30 cycles, both charge and discharge capacities decrease slowly in the subsequent cycles and remain nearly constant with coulombic efficiency of higher than 97 %. After 150 cycles, the reversible capacity retains as high as 665 mA h g^{-1}. The thin conductive PPy layer

could not only prevent direct contact between Fe_2O_3 and electrolyte, but also inhibit the outward expansion of Fe_2O_3, thus improving the structural integrity of the electrode and facilitating the stability of SEI film formed on the surfaces, which is beneficial to the enhanced electrochemical performances.

Rate performances of the two samples are presented in Fig. 7. Fe_2O_3@PPy nanotube arrays deliver the discharge capacities of 861, 694, 592, and 455 mA h g^{-1} at current densities of 100, 200, 400, and 800 mA g^{-1} every 10
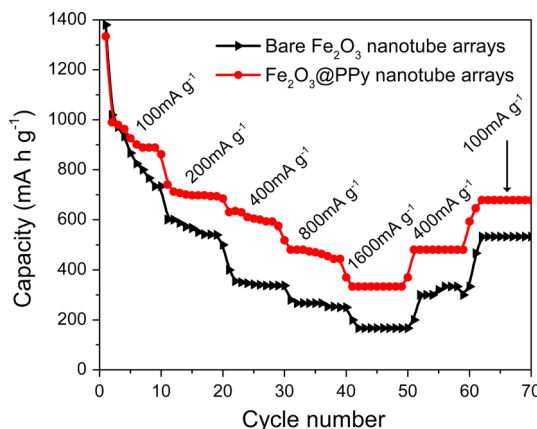
Fig. 7 Rate performances of bare Fe_2O_3 and Fe_2O_3@PPy nanotube arrays' electode

cycles, respectively. Even at a high current density of 1600 mA g^{-1}, the specific capacity still retains a value of 333 mA h g^{-1} and rebounds to 678 mA h g^{-1} when the current density is reset to 100 mA g^{-1}, indicating the excellent tolerance against the high current density of Fe_2O_3 @PPy nanotube arrays' electrode. In comparison, the capacity of bare Fe_2O_3 nanotube arrays decreases more dramatically to 167 mA h g^{-1} at a current density of 1600 mA g^{-1} after 50 cycles.

It has been proposed that the cycle stability and high rate capability are mainly related to the thickness of SEI film, interfacial charge-transfer process, and lithium–ion diffusion in a composite. To gain further insight into the electrochemical performance, electrochemical impedance spectroscopy (EIS) measurements were carried out at room temperature on the cells after the first and 150 cycles, respectively, at the fully delithiation state. The complex plane plots for each sample can be divided into high-frequency semicircle and low-frequency sloping line (Fig. 8a, b). The intercepts at the real impedance (Z′) axis in the high-frequency region are generally considered as electrical conductivities of the electrode, the electrolyte, and the separator [46], and it remains almost constant after 150 cycles for both electrodes. The diameter of the semicircle in the high-frequency range is correlated to the resistance of SEI layer formed on the surface of electrode (R_{sf}) and to the charge-transfer resistance (R_{ct}) between the surface films and the active material [16]. No obvious difference of $R_{(sf+ct)}$ between the two sample can be seen after one cycle. However, the $R_{(sf+ct)}$ of bare Fe_2O_3 nanotube arrays is much higher than that of Fe_2O_3@PPy after 150 cycles, which could be attributed to the stable structure of Fe_2O_3 @PPy nanotube arrays, demonstrating that PPy could promote charge transfer and improve the electrochemical performance of anode. Furthermore, in the low-frequency area, the phase angle for impedance plot of the Fe_2O_3@PPy nanotube arrays is much higher than that of the bare Fe_2O_3 nanotube arrays, indicating a faster Li^+ diffusion in the

Fe_2O_3@PPy nanotube's structure during repeated charge/discharge processes.

To check the valence state of iron after the coulombic efficiency becomes roughly constant, the Fe2p3/2 XPS high-resolution spectra of bare Fe_2O_3 and Fe_2O_3@PPy electrodes after the 35th cycling at fully delithiation state were recorded. For both electrodes, the polymer layers on the surface were removed by scotch tape method in a glove box prior to analysis to expose the interior of the electrodes [47]. As shown in Fig. 9, the peaks at 710.9 and 709.7 eV are assigned to Fe^{3+} in an oxide matrix (Fe_2O_3 and/or Fe_3O_4); the peak at 708.3 eV is attributed to Fe^{2+} in an oxide matrix (Fe_3O_4); and the minor component at 714.3 eV is attributed to a Fe^{2+} 2p3/2 satellite [39, 48, 49]. As can be observed, although the peak intensity of Fe^{3+} is much larger than that of Fe^{2+} in both electrodes, the proportion of Fe^{3+}–Fe^{2+} in Fe_2O_3@PPy electrode (Fig. 9b) is higher compared to that of the bare Fe_2O_3 electrode (Fig. 9a), indicating a lower content of Fe^{2+}. The presence of Fe^{2+} in the electrode after cycling may be caused by the incompletely restored of hematite (Fe^{3+}) during the delithiation process in the initial several cycles. Li^+ would be trapped in the anode material along with the formation of Fe^{2+}, and the capacity would decrease [37]. The lower content of Fe^{2+} in Fe_2O_3@PPy electrode is due to the faster transport of both Li^+ and electrons during repeated charge/discharge processes, which is beneficial for the good reversibility of the electrochemical reactions.

The enhanced structure and surface stabilization are demonstrated through SEM investigation. Figure 10 shows the SEM images of bare Fe_2O_3 and Fe_2O_3@PPy nanotube arrays after 150 cycles at a current density of 100 mA g^{-1}. After the lithiation/delithiation cycles, the surface of Fe_2O_3 @PPy nanotubes becomes rough with a modest increase of around 50 nm in diameter, but the morphology remains the same as before (Fig. 10b). On the contrary, the lithiated bare Fe_2O_3 nanotubes suffer a dramatic radial expansion with huge crack and pulverization phenomenon (Fig. 10a),

Fig. 8 The EIS spectra of bare Fe_2O_3 and Fe_2O_3@PPy nanotube arrays' electrode after **a** the first and **b** 150 cycles, respectively
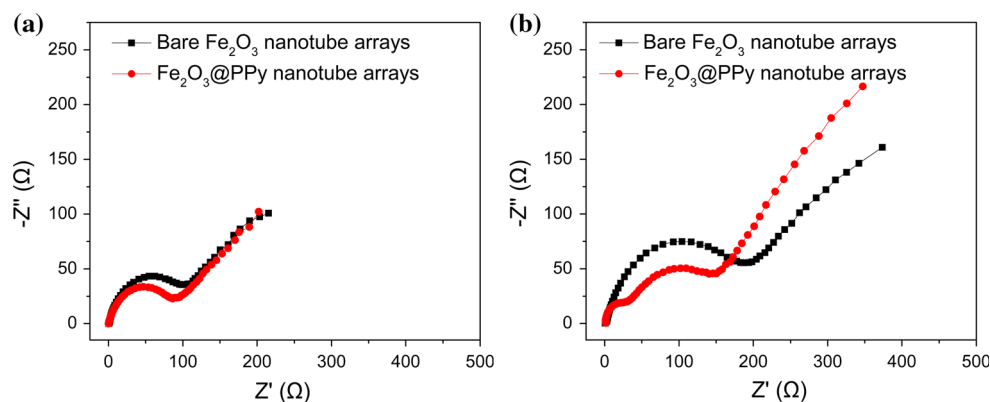
Fig. 9 XPS high-resolution spectra of Fe2p3/2 core level for **a** bare Fe_2O_3 and **b** Fe_2O_3@PPy nanotube arrays' electrode after 35 cycles
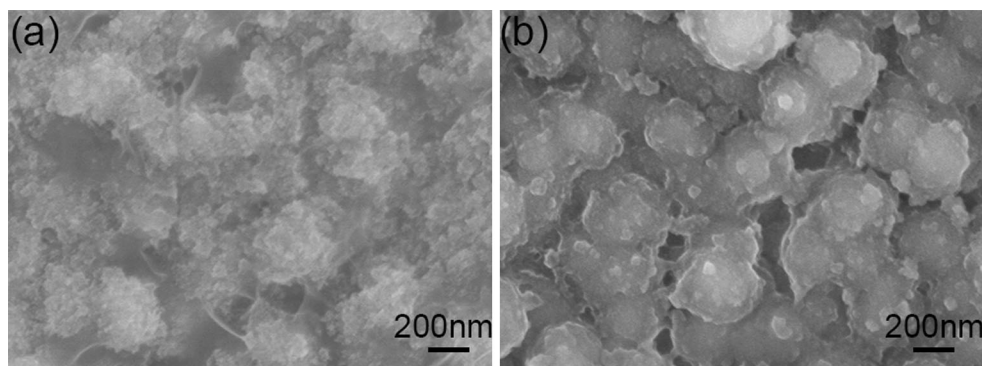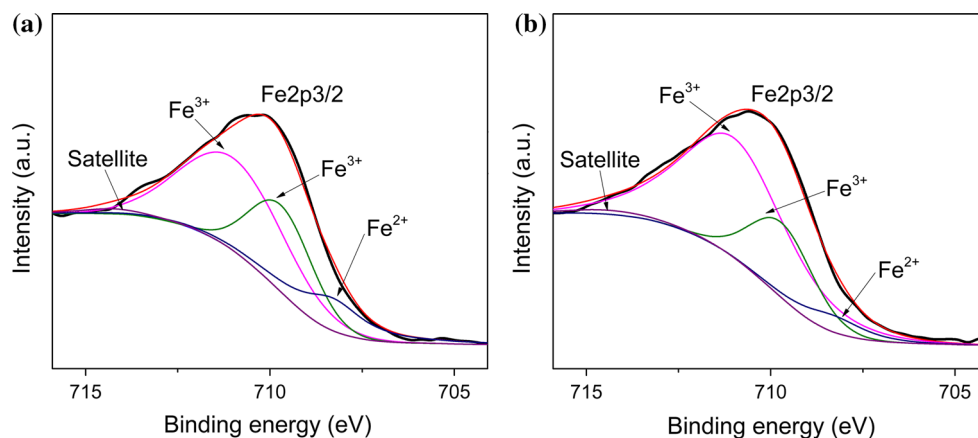

Fig. 10 SEM images of **a** bare Fe_2O_3 and **b** Fe_2O_3@PPy nanotube arrays' electrodes after 150 cycles

leading to the formation of thick SEI films which would cause the consumption of more Li^+ and a large irreversible capacity.

Overall, several factors have contributed to the excellent electrochemical performance of hybrid nanotube arrays' electrode. First, the well-defined hollow nanotube structure is capable of providing larger materials/electrolyte interface for faster reaction kinetics. Second, the introduction of PPy and the direct connection with the current collector can improve the electronic conductivity and provide an elastic protection to keep the integrity of the structure. Last but not the least, the homogenous coating of PPy is beneficial to form a stable SEI film, which could suppress the detrimental surface effects on the electrode, leading to the improved cycling characteristics.

Conclusions

We have designed and assembled a novel nanostructure of PPy coating on hollow Fe_2O_3 nanotube arrays for electrode material. In this well-engineered hybrid architecture, the preferred structures of each component are thoroughly conducive to guarantee highways for electron transport and maintain excellent structural/interfacial stability. By combining such fascinating advantages of ordered 3D Fe_2O_3 nanotube arrays and conductive PPy layer, the electrode exhibits superior electrochemical stability and high rate performance. Besides, the morphology is well preserved after repeated Li^+ insertions and extractions. This 3D hybrid nanostructure might open new avenues for the design of other high-performance cathode and anode electrode materials.

References

1. Guo JX, Chen L, Wang GJ, Zhang X, Li FF (2014) In situ synthesis of SnO_2-Fe_2O_3@polyaniline and their conversion to SnO_2-Fe_2O_3@C composite as fully reversible anode material for lithium-ion batteries. J Power Sour 246:862–867
2. Jiang SH, Yue WB, Gao ZQ, Ren Y, Ma H, Zhao XH, Liu YL, Yang XJ (2013) Graphene-encapsulated mesoporous SnO_2 composites as high performance anodes for lithium-ion batteries. J Mater Sci 48:3870–3876. doi:10.1007/s10853-013-7189-9

3. Xu WW, Zhao KN, Niu CJ, Zhang L, Cai ZY, Han CH, He L, Shen T, Yan MY, Qu LB, Mai LQ (2014) Heterogeneous branched core-shell SnO_2-PANI nanorod arrays with mechanical integrity and three dimensional electron transport for lithium batteries. Nano Energy 8:196–204

4. Liu H, Wang GX, Park J, Wang JZ, Liu HK, Zhang C (2009) Electrochemical performance of α-Fe_2O_3 nanorods as anode material for lithium-ion cells. Electrochim Acta 54:1733–1736

5. Wang W, Bu FX, Jiang JS (2015) Porous TiO_2 coated α-Fe_2O_3 ginger-like nanostructures with enhanced electrochemical properties. Mater Lett 139:89–92

6. Chen MH, Liu JL, Chao DL, Wang J, Yin JH, Lin JY, Fan HJ, Shen ZX (2014) Porous α-Fe_2O_3 nanorods supported on carbon nanotubes-graphene foam as superior anode for lithium ion batteries. Nano Energy 9:364–372

7. Wang RH, Xu CH, Sun J, Gao L, Lin CC (2013) Flexible freestanding hollow Fe_3O_4/graphene hybrid films for lithium-ion batteries. J Mater Chem A 1:1794–1800

8. Wu Z-S, Ren WC, Wen L, Gao LB, Zhao JP, Chen ZP, Zhou GM, Li F, Cheng H-M (2010) Graphene anchored with Co_3O_4 nanoparticles as Anode of lithium ion batteries with enhanced reversible capacity and cyclic performance. ACS Nano 4:3187–3194

9. Jin YH, Li Wang, Shang YM, Gao J, Li JJ, He XM (2015) Facile synthesis of monodisperse Co_3O_4 mesoporous microdisks as an anode material for lithium ion batteries. Electrochim Acta 151:109–117

10. Szabo DV, Kilibarda G, Schlabach S, Trouillet V, Bruns M (2012) Structural and chemical characterization of SnO_2-based nanoparticles as electrode material in Li-ion batteries. J Mater Sci 47:4383–4391. doi:10.1007/s10853-012-6292-7

11. Cao F, Pan GX, Xia XH, Tang PS, Chen HF (2014) Synthesis of hierarchical porous NiO nanotube arrays for supercapacitor application. J Power Sour. 264:161–167

12. Chen J, Xu LN, Li WY, Gou XL (2005) α-Fe_2O_3 nanotubes in gas sensor and lithium-ion battery applications. Adv Mater 17:582–586

13. Su QM, Xie D, Zhang J, Du GH, Xu BS (2013) In situ transmission electron microscopy observation of the conversion mechanism of Fe_2O_3/graphene anode during lithiation-delithiation processes. ACS Nano 7:9115–9121

14. Zou MZ, Li JX, Wen WW, Chen LZ, Guan LH, Lai H, Huang ZG (2014) Silver-incorporated composites of Fe_2O_3 carbon nanofibers as anodes for high-performance lithium batteries. J Power Sour 270:468–474

15. Wang BB, Wang G, Wang H (2015) Synthesis and electrochemical investigation of hollow hierarchical metal oxide microspheres for high performance lithium-ion batteries. Electrochim Acta 156:1–10

16. Fan X, Dou P, Jiang AN, Ma DQ, Xu XH (2014) One-step electrochemical growth of three-dimensional Sn-Ni@PEO nanotube array as a high performance lithium-ion battery anode. ACS Appl Mater Interfaces 6:22282–22288

17. Zeng WQ, Zheng FP, Li RZ, Zhan Y, Li YY, Liu JP (2012) Template synthesis of SnO_2/α-Fe_2O_3 nanotube array for 3D lithium ion battery anode with large areal capacity. Nanoscale 4:2760–2765

18. Lamberti A, Garino N, Sacco A, Bianco S, Chiodoni A, Gerbaldi C (2015) As-grown vertically aligned amorphous TiO_2 nanotube arrays as high-rate Li-based micro-battery anodes with improved long-term performance. Electrochim Acta 151:222–229

19. Wang B, Qiu TF, Li XL, Luo B, Hao L, Zhang YB, Zhi LJ (2015) Synergistically engineered self-standing silicon/carbon composite arrays as high performance lithium battery anodes. J Mater Chem A 3:494–498

20. Wu H, Chan G, Choi JW, Ryu I, Yao Y, Mcdowell MT, Lee SW, Jackson A, Yang Y, Hu LB, Cui Y (2012) Stable cycling of double-walled silicon nanotube battery anodes through solid-electrolyte interphase control. Nat Nanotech 7:310–315

21. Balaya P, Li H, Kienle L, Maier J (2003) Fully reversible homogeneous and heterogeneous Li storage in RuO_2 with high capacity. Adv Funct Mater 13:621–625

22. Hu J, Li H, Huang XJ, Chen LQ (2006) Improve the electrochemical performances of Cr_2O_3 anode for lithium ion batteries. Solid State Ion 177:2791–2799

23. Han F, Li D, Li WC, Lei C, Sun Q, Lu AH (2013) Nanoengineered polypyrrole-coated Fe_2O_3@C multifunctional composites with an improved cycle stability as lithium-ion anodes. Adv Funct Mater 23:1692–1700

24. Fu LJ, Liu H, Li C, Wu YP, Rahm E, Holze R, Wu HQ (2006) Surface modifications of electrode materials for lithium ion batteries. Solid State Sci 8:113–128

25. Li S, Qin XY, Zhang HR, Wu JX, He Y-B, Li BH, Kang FY (2014) Silicon/carbon composite microspheres with hierarchical core-shell structure as anode for lithium ion batteries. Electrochem Commun 49:98–102

26. Gowda SR, Reddy ALM, Shaijumon MM, Zhan XB, Ci LJ, Ajayan PM (2011) Conformal coating of thin polymer electrolyte layer on nanostructured electrode materials for three-dimensional battery applications. Nano lett 11:101–106

27. Yoon T, Chae CJ, Sun Y-K, Zhao X, Kung HH, Lee JK (2011) Bottom-up in situ formation of Fe_3O_4 nanocrystals in a porous carbon foam for lithium-ion battery anodes. J Mater Chem 21:17325–17330

28. Xu WW, Zhao KN, Niu CJ, Zhang L, Cai ZY, Han CH, He L, Shen T, Yan MY, Qu LB, Mai LQ (2014) Heterogeneous branched core-shell SnO_2-PANI nanorod arrays with mechanical integrity and three dimensional electron transport for lithium batteries. Nano Energy 8:196–204

29. Cui LF, Shen J, Cheng FY, Tao ZL, Chen J (2011) SnO_2 nanoparticles@polypyrrole nanowires composite as anode materials for rechargeable lithium-ion batteries. J Power Sour 196:2195–2201

30. Nyholm L, Nystrom G, Mihranyan A, Stromme M (2011) Toward flexible polymer and paper-based energy storage devices. Adv Mater 23:3751–3769

31. Liu JL, Zhou WW, Lai LF, Yang HP, Lim SH, Zhen YD, Yu T, Shen ZX, Lin JY (2013) Three dimensionals α-Fe_2O_3/polypyrrole (Ppy) nanoarray as anode for micro lithium ion batteries. Nano energy 2:726–732

32. Song T, Xia JL, Lee J-H, Lee DH, Kwon M-S, Choi J-M, Wu J, Doo SK, Chang H, Park W, Zang DS, Kim H, Huang YG, Hwang K-C, Rogers JA, Paik U (2010) Arrays of sealed silicon nanotubes as anodes for lithium ion batteries. Nano Lett 10:1710–1716

33. Lotfabad EM, Kalisvaart P, Kohandehghan A, Cui K, Kupsta M, Farbod B, Mitlin D (2014) Si nanotubes ALD coated with TiO_2, TiN or Al_2O_3 as high performance lithium ion battery anodes. J Mater Chem A 2:2504–2516

34. Desai UV, Xu CK, Wu JM, Gao D (2013) Hybrid TiO_2-SnO_2 nanotube arrays for dye-sensitized solar cells. J Phys Chem C 117:3232–3239

35. Liu JP, Li YY, Fan HJ, Zhu ZH, Jiang J, Ding RM, Hu YY, Huang XT (2010) Iron oxide-based nanotube arrays derived from sacrificial template-accelerated hydrolysis: large-area design and reversible lithium storage. Chem Mater 22:212–217

36. Liu JP, Huang XT, Li YY, Ji XX, Li ZK, He X, Sun FL (2007) Vertically aligned 1D ZnO nanostructures on bulk alloy substrates: direct solution synthesis, photoluminescence, and field emission. J Phys Chem C 111:4990–4997

37. Lv XX, Deng JJ, Wang J, Zhong J, Sun XH (2015) Carbon-coated α-Fe$_2$O$_3$ nanostructures for efficient anode of Li-ion battery. J Mater Chem A 3:5183–5188

38. Liu RQ, Li DY, Wang C, Li N, Li Q, Lu XJ, Spendelow JS, Wu G (2014) Core-shell structured hollow SnO$_2$-polypyrrole nanocomposite anodes with enhanced cyclic performance for lithium-ion batteries. Nano Energy 6:73–81

39. Wu C, Zhang H, Wu YX, Zhuang QC, Tian LL, Zhang XX (2014) Synthesis and characterization of Fe@Fe2O3 core-shell nanoparticles/graphene anode material for lithium-ion batteries. Electrochim Acta 134:18–27

40. Chen G, Rodriguez R, Fei L, Xu Y, Deng SG, Smirnov S, Luo HM (2014) A facile hydrothermal route to iron(III) oxide with conductive additives as composite anode for lithium ion batteries. J Power Sour 259:227–232

41. Liang K, Gu TL, Cao ZY, Tang XZ, Hu WC, Wei BQ (2014) In situ synthesis of SWNTs@MnO$_2$/polypyrrole hybrid film as binder-free supercapacitor electrode. Nano Energy 9:245–251

42. Zhao JF, Zhang SC, Liu WB, Du ZJ, Fang H (2014) Fe$_3$O$_4$/PPy composite nanospheres as anode for lithium-ion batteries with superior cycling performance. Electrochim Acta 121:428–433

43. Cherian CT, Sundaramurthy J, Kalaivani M, Ragupathy P, Kumar PS, Thavasi V, Reddy MV, Sow CH, Mhaisalkar SG, Ramakrishna S, Chowdari BVR (2012) Electrospun α-Fe$_2$O$_3$ nanorods as a stable, high capacity anode material for Li-ion batteries. J Mater Chem 22:12198–12204

44. Sun B, Horvat J, Kim HS, Kim W-S, Ahn J, Wang GX (2010) Synthesis of mesoporous α-Fe$_2$O$_3$ nanostructures for highly sensitive gas sensors and high capacity anode materials in lithium ion batteries. J Phys Chem C 114:18753–18761

45. Shin J-Y, Samuelis D, Maier J (2011) Sustained lithium-storage performance of hierarchical, nanoporous anatase TiO$_2$ at high rates: emphasis on interfacial storage phenomena. Adv Funct Mater 21:3464–3472

46. Wei DH, Liang JW, Zhu YC, Zhang JJ, Li XN, Zhang KL, Yuan ZQ, Qian YT (2013) Facile formation of graphene-encapsulated α-Fe$_2$O$_3$ nanorice as enhanced anode materials for lithium storage. Electrochim Acta 114:779–784

47. Lotfabad EM, Kalisvaart P, Kohandehghan A, Karpuzov D, Mitlin D (2014) Origin of non-SEI related conlombic efficiency loss in carbons tested against Na and Li. J Mater Chem A 2:19685–19695

48. Tian BB, Swiatowska J, Maurice V, Zanna S, Seyeux A, Klein LH, Marcus P (2013) Combined surface and electrochemical study of the lithiation/delithiation mechanism of the iron oxide thin-film anode for lithium-ion batteries. J Phys Chem C 117:21651–21661

49. Kaya S, Ogasawara H, Nilsson A (2015) Determination of the surface electronic structure of Fe$_3$O$_4$(111) by soft X-ray spectroscopy. Catal Today 240:184–189